Effects of Nasal Cavity and Exhalation Dynamics on Aerosol Spread in Simulated Respiratory Events

Nicolás Catalán, Salvatore Cito*, Sylvana Varela, Alexandre Fabregat, Anton Vernet,
Jordi Pallarès

Departament d'Enginyeria Mecànica. Universitat of Rovira i Virgili, Av. Països Catalans,
26, 43007 – Tarragona, Spain.
*Corresponding author: salvatore.cito@urv.cat

Abstract

Coughing and sneezing are critical mechanisms for the transmission of airborne respiratory diseases, dispersing pathogen-laden aerosols into the environment. Previous human volunteer studies provided valuable insights into aerosol dynamics but lacked reproducibility due to individual variations. This paper presents a novel, replicable experimental setup using three dimensional (3D) models of the upper respiratory tract and nasal cavity to simulate isothermal human-like coughs and sneezes. Results indicate that nasal cavity involvement decreases horizontal aerosol cloud spread while enhancing vertical dispersion. Incorporating this experimental data with theoretical models improves predictive accuracy of aerosol cloud evolution, particularly for indoor environments. Finally, a single novel analytical expression for the evolution of the particle cloud tip is derived that accurately predicts the cases studied.

1. Introduction

The SARS-CoV2 pandemic, with over 650 million confirmed cases and 7 million deaths,[1] tragically highlighted the critical need to understand how respiratory diseases spread through airborne aerosols (microscopic droplets expelled during breathing, coughing, and sneezing).[2–5] Accurately replicating these events in research settings is crucial for developing effective mitigation strategies. However, a key limitation of current methods lies in the use of human volunteers.[6–8] Individual differences in cough/sneeze strength and anatomy limit the robust characterization of exhalation flows and the resulting aerosol cloud. This variability also hinders the development of reliable models for cloud dispersion.[6] To overcome these limitations, researchers are turning to replicable cough and sneeze simulators (both numerical and experimental) which offer several advantages over volunteer-based studies in terms of reproducibility and accuracy. These cough and sneeze emulators enable the controlled generation of rapid exhalations with adjustable parameters that allow researchers to conduct standardized experiments, ensuring consistent and reproducible data collection. A critical factor in accurately representing cough and sneeze events is incorporating realistic upper respiratory tract within the simulator. Since coughs and sneezes air can be expelled through both the mouth and the nose,[3] these models should include both cavities and respective airways along with the larynx and trachea.[9,10]

In this regard, the nasal cavity plays a crucial role in shaping the airflow dynamics and particle cloud dispersion influencing the size, direction, and dispersion rate of the expelled droplets and, therefore, potentially impacting the spread of pathogens.[9] Previous studies have characterized airflow and particle size distribution during coughs and sneezes using various techniques like spirometry and Particle Image Velocity (PIV).[6–8,11,12] These studies have revealed key insights on flow rates, particle velocities, and droplet size distributions. Researchers have also developed theoretical models to predict particle cloud evolution and droplet size based on factors like humidity and composition.[13–15] In this case, neglecting the nasal cavity can result in an incomplete understanding of airflow dynamics and particle dispersion patterns, impacting the accuracy of transmission models.[2,16,17] Efforts specifically aimed at measuring differences between the nasal and oral routes have reported changes in droplet characteristics, droplet travel distance, airborne duration, and pathogen-carrying potential.[18] The nasal cavity flow has also been found to modify the pathogen's capacity to adhere to mucosal surfaces.[19,20]

To overcome the limitations, we designed and built a replicable cough and sneeze simulator. This novel experimental setup is used here to generate exhalations resembling human coughs and sneezes with adjustable parameters used to control the air ejection strength using the maximum velocity peak and duration of the simulated expiratory event. Using realistic 3D printed models of the upper respiratory tract and nasal cavity, we can investigate the role of the exhalation strength and the role of nasal airways (by blocking or not the nostrils of the model) on the aerosol cloud dispersion.

The objective of this study is to characterize experimentally, in a controlled and reproducible way, the aerosol cloud generated in a violent expiratory event. The collected experimental data, comprising three different flow rates, typical of coughs and sneezes, with and without nasal cavity flow are used to determine the entrainment coefficient of the jet flow and predict the range of the aerosol cloud using the model proposed by Pallares and Fabregat.[21] A single correlation, experimentally validated, to predict the time evolution of the position of the tip of the cloud is proposed.

2. Materials and methods

2.1. Experimental setup

The experimental setup, sketched in Figure 1, consists of a compressor, a pressurized small tank with an electro valve and a relief valve, a plenum tank, a ball valve, a pipe, a pressure differential sensor, two flexible tubes, a mixing chamber, a nebulizer, and a 3D printed model of the upper respiratory tract and nasal cavity (see Fig. 2). The computer-controlled compressor, relief valve and electro valves allow to select target conditions for the exhalation.

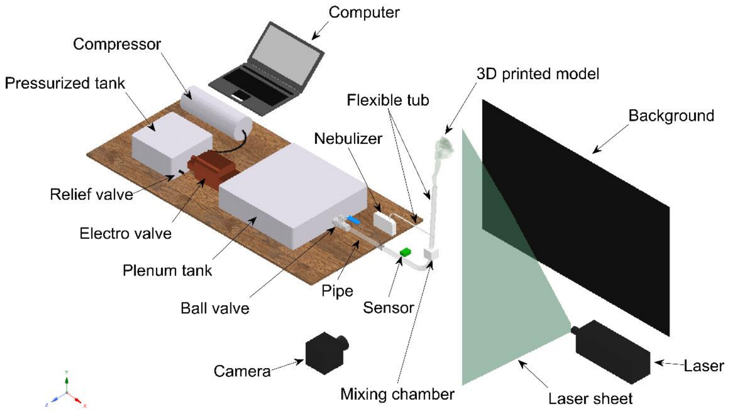

Figure 1. Sketch of the experimental setup.

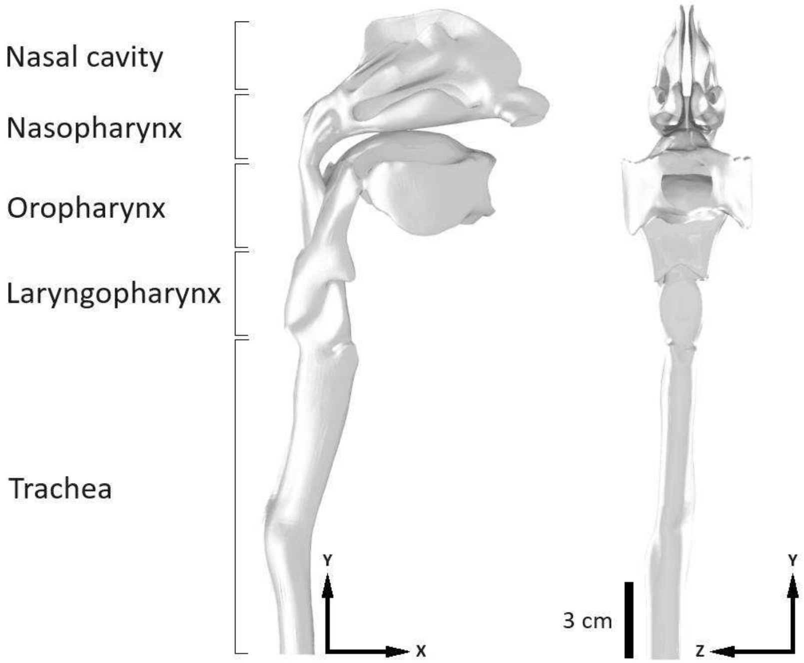

Figure 2. Lateral (left) and front (right) views of the 3D printed model of the upper respiratory tract and trachea.

To initialize the expiratory event, the following steps are taken: first, we select the desired pressure (hPa) in the pressurized tank with a volume of 4.1 liters. The relief valve is used to regulate the overpressure inside the box. Once the pressure reaches the set point, the electro valve is opened and the air flows to the plenum tank with a volume of 1.3 liters. The opening of the ball valve (3/4”) controls the duration of the simulated expiratory event letting the air to flow through a pipe of 75 cm long (Internal diameter of 16 mm). The pressure difference under fully-developed conditions is obtained from measurements at two points separated 10 cm using a calibrated SMI ultra-low pressure digital sensor (model SM9333 BCE-T-125-000) working at 1000 Hz. Microdroplets, with an average diameter of 1 μm generated with a nebulizer (Aroma Nebulizer 2.0), are introduced into the mixing chamber through a flexible tube 40 cm long (ID 8 mm) where the mixture is homogenized. A 50 cm long (ID 20 mm) flexible tube connects the mixing chamber with the 3D printed upper respiratory tract model as shown in Figure 1. The trachea and the upper respiratory tract of the model (see Fig. 2) were obtained from the ERCOFTAC database[22] while the nasal cavity, corresponding to an average geometry for 25 volunteers, was retrieved from Brüning *et al.*[23] The open area of the mouth (3.14 cm^2) is circular with a diameter of 2 cm and the total area of the two nostrils is 1.99 cm^2. When the nostrils are open, the total flow rate is distributed proportionally between the open areas of the mouth and nostrils, with 61% passing through the mouth and 39% through the nostrils. This distribution has been validated at various flow rates using numerical simulations of airflow within the geometry of the upper respiratory tract considered in this study. The flow rate measurements have a maximum error margin of ± 5%.

The temperature in the laboratory, with dimensions 8.5 x 5 x 4 m^3 (length x width x height) was kept at 25^{o}C during the measurements. The evolution of the particle cloud was obtained using a 5 mm thick laser sheet generated by a continuous green laser (CNI Model with PSU-W-LED MGL-W-532, wavelength: 532 nm). Images of an area of 1.27 x 1.59 m^2 were acquired using a digital camera (Photron FASTCAM mini UX100 type 800K) running at 50 FPS with a resolution of 1280 x 1024 pixels for a period of 1.5 s. The postprocessing of the images was performed using an in-house Matlab code. The cloud contours were obtained by binarizing each frame using a constant threshold. Figure 2 shows the coordinate system where x is the axial direction, y is the vertical direction and z is the transversal direction. The particle cloud centroid coordinates in the illuminated x-y plane (c_x, c_y), and the horizontal (σ_x) and vertical (σ_y) widths are estimated using the standard deviation defined in Eqs. 1 and 2, respectively.

$$c_x = \frac{\sum_{i=1}^{n} x_i}{n}, c_y = \frac{\sum_{i=1}^{n} y_i}{n} \tag{1}$$

$$\sigma_x = \sqrt{\frac{\sum_{i=1}^{n}(x_i - c_x)^2}{n}}, \sigma_y = \sqrt{\frac{\sum_{i=1}^{n}(y_i - c_y)^2}{n}}, \tag{2}$$

where *n* is the number of illuminated pixels in the binarized image, x_i is the horizontal pixel position and y_i is the vertical pixel position.

3. Results and discussion

3.1 Experimental results

To investigate the impact of the nasal cavity flow and exhalation strength, we conducted six different experimental cases, as listed in Table 1. The three different flow rates are identified by the first two digits of the case code, namely, F1, F2 and F3. The last two digits of the code, either N0 or N1, correspond to closed or open nostrils, respectively. Therefore, for instance, the case F2N0 would correspond to the second flow rate and closed nostrils. For each case, Table 1 shows the total flow rate in liters per second, the exhalation duration in seconds, the maximum velocity in meters per second and the nostril openness (for further information see Appendix II). To estimate the statistical variability of the different realizations of the same turbulent flow, each case was repeated 10 times. The results for each case presented and discussed in this section are obtained from the ensemble average of the 10 realizations.

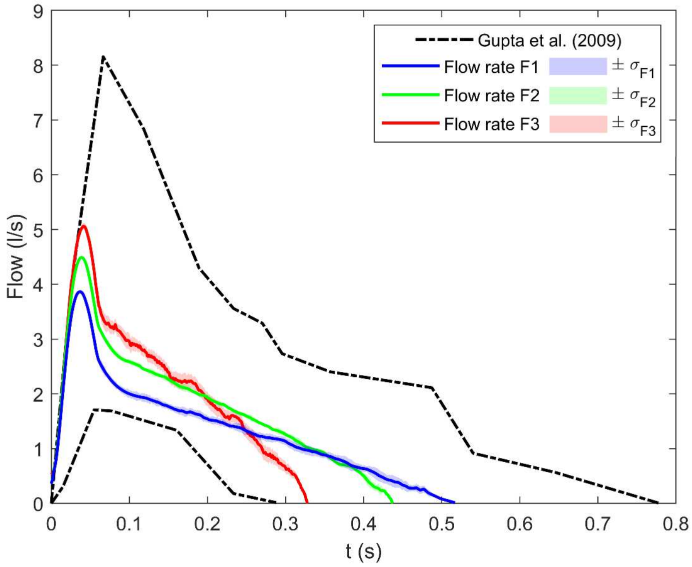

Figure 3. Temporal evolution of the ensemble-averaged volumetric flow rate for the three experiments (solid lines), with one deviation standard of 10 realizations for each case (shaded areas), and the envelopes of the measurements reported by Gupta *et al.*[6] (dashed lines).

The temporal evolution of the exhalation flow rate for the three experiments (F1, F2, and F3) are shown in Figure 3 with solid lines, while the shaded area represents the variability of ± 5%, corresponding to plus/minus one standard deviation, calculated from 10 independent realizations. For validation purposes, the dashed line corresponds to the envelope of the different measurements, reported by Gupta *et al.*[6], of coughs flows of volunteers. The general trend of the present results shown in Figure 3 are very similar to those reported by Gupta *et al.*[6] with a rapid increase in flow rate that peaks shortly after the onset of the exhalation that then transitions to a slower decay until termination. In comparison to other studies[7,8] on the characterization of sneezes, the present experiment airflow velocities are in very good agreement with values ranging between 10 and 18 m/s as well, allowing coughing and sneezing to be studied interchangeably.

PLEASE CITE THIS ARTICLE AS DOI: 10.1063/5.0241346

Code	Total flow rate (l/s)		Duration (s)	Max velocity (m/s)	Nostrils	
	Max.	Av.	t_d	Mouth	Closed	Open
F1N0	3.82	1.34	0.50	12,16	X	
F1N1						X
F2N0	4.44	1.77	0.44	14,14	X	
F2N1						X
F3N0	5.04	2.09	0.34	16,05	X	
F3N1						X

Table I. Experimental conditions.

Figure 4 compares the temporal evolution of the position of the centroid and the vertical and horizontal widths of the aerosol for flow rates F1 (blue) and F2 (gray) with closed (N0) and open (N1) nasal airways over 1.5 seconds. Panels a (N0) and b (N1) correspond to the horizontal position of the centroid and horizontal width of the cloud. The corresponding vertical metrics of the cloud and shown in panels c) and d). The middle solid line in panels a) and b) correspond the c_x, the dashed line represents $+\sigma_x$ while the pointed line indicates the $-\sigma_x$. Note that the vertical axis corresponds to elapsed time. The vertical cloud centroid position and width are similarly shown in panels c) and d) with elapsed time in the horizontal axis. Shaded areas show the one standard deviation for the ensemble of 10 experimental realizations for each case.

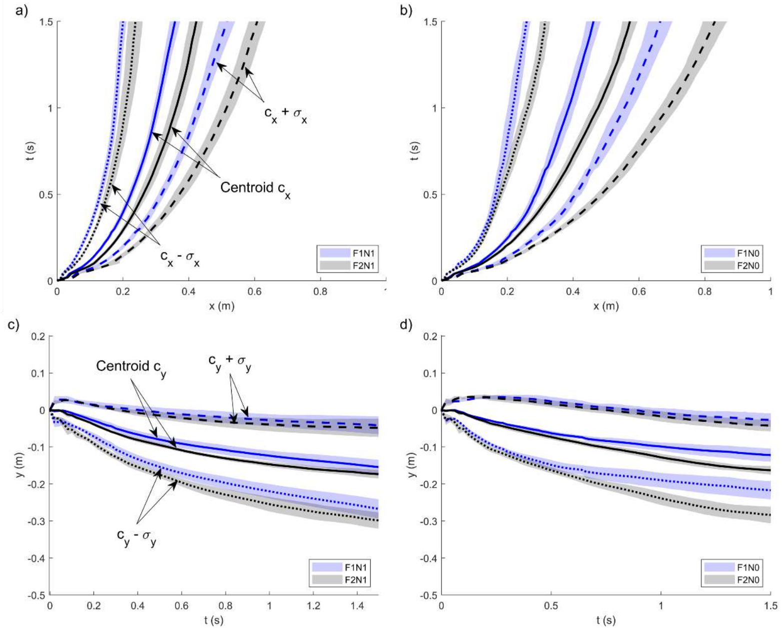

Figure 4. Tracking of the position of the ensemble-averaged centroid and time evolutions of the sizes of particle clouds for cases (a and c) F1N1 F2N1 and (b and d) F1N0 F2N0.

Considering F1 as the base case, results indicate that the increased flow rate in case F2 leads to larger horizontal reach for both cases N1 (panel a) and N0 (panel b). Increasing the total amount of exhaled air leads to increased traveled distance in the horizontal axis and also a slightly larger variability across all experiments in the ensemble as indicated by the modestly wider shaded area. The existence of nasal flow has also a clear impact on the cloud horizontal reach. Comparison of panels a) and b) show that the interaction of the main (mouth) and the oblique nasal jet leads to a reduction in the horizontal distance travelled by the particle cloud. This reduction might have a two-fold explanation. On the one hand, the quasi-forward oriented mouth jet in cases N0 is generated by a smaller fraction of air that now splits between the two airways. Additionally, the nasal ejection disturbs the mouth jet by deflecting it downwards and accelerating the decay of the kinetic energy along the horizontal axis. These findings demonstrate how nasal exhalation can reduce the horizontal transmission distance of aerosols, which may have implications for designing protective measures in close-contact settings.

In the vertical direction (panels c and d), the data suggest that increasing the flow rate has only a modest effect on the vertical movement of the aerosol cloud. When comparing to the baseline case (F1), the addition of nasal flow similarly has minimal influence on the cloud's descent, maintaining a relatively stable vertical centroid position. This limited vertical shift, despite increased flow or nasal involvement, suggests that while nasal airflow affects horizontal spread significantly, its role in vertical dispersion is comparatively minor. This could indicate that aerosols expelled through the nose are less likely to rise or fall dramatically in the immediate aftermath of exhalation, focusing their spread more horizontally, which could be important for understanding near-field transmission in indoor environments.

The differences observed between case F2 and the reference F1 (see Figure 4), exacerbate when the flow rate is further increased in case F3 (red) as shown in Figure 5. On the one hand, the largest flow rate in case F3 results in the largest horizontal reach and increased variability in both cloud centroid position and width as shown in panels a) and b). Again, the existence of nasal flow results in an increased cloud horizontal travelled distance that reaches the maximum value for case F3.

Regarding the vertical direction, the impact of both increased flow rate and nasal flow in case 3 is much more obvious than in case 2 (see Figure 4) with both the cloud centroid and width exhibiting significantly larger values. While the effect of nasal flow on the cloud descent was very modest in Figure 4, results in Figure 5 for case 3 clearly show the signature of this oblique jet on the vertical span of the cloud.

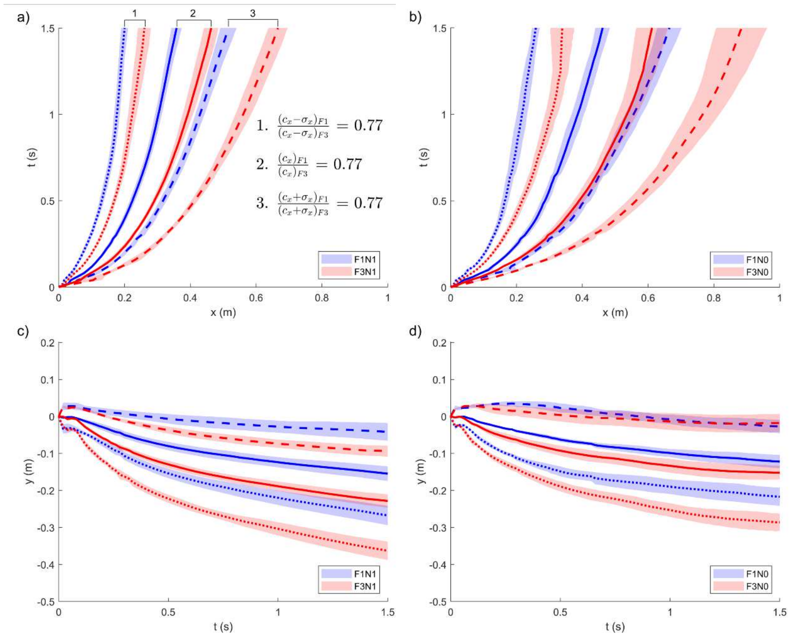

Figure 5. Tracking of the position of the ensemble-averaged centroid and time evolutions of the sizes of particle clouds for cases (a and c) F1N1 F3N1 and (b and d) F1N0 F3N0.

Table II and Figure 5 (a) show the ratio between the position and sizes of the cloud for the different flow rates at the axial direction in both closed (N0) and open (N1) nostrils. The ratio of the flow rates and the ratio of distances are in both similar, with a maximum error of 4.34 % between the ratio of the flow rate and the size. A similar scaling has not been found for the vertical metrics.

Code	Flow rate ratio	N0			N1			Size ratio avg.	Difference % in abs. value
		c_x - σ_x ratio	c_x ratio	c_x + σ_x ratio	c_x - σ_x ratio	c_x ratio	c_x + σ_x ratio		
F1/F2	0.86	0.82	0.81	0.80	0.87	0.85	0.85	F1 = 0.83F2	3.61
F1/F3	0.75	0.76	0.75	0.75	0.77	0.77	0.77	F1 = 0.76F3	1.31
F2/F3	0.88	0.93	0.93	0.94	0.91	0.91	0.91	F2 = 0.92F3	4.34

Table II. Flow rate ratio and difference of the distances of the puff between the cases compared.

The cloud average centroid trajectories are plotted in Figure 6 using colored solid and dashed lines for the cases with and without nasal flow, respectively. Results suggest that despite differences in the total travelled length, flow rate has a limited impact on the path followed by the particle cloud centroid over 1.5 s. The existence of nasal flow, however, clearly affects the deflection angle of the trajectory that increases from about $\alpha_{N0} = 18°$ to $\alpha_{N1} = 30°$, regardless of the flow rate and the duration of the flow injection. The black lines show the evolution of the centroid trajectory angle of the thermal field obtained in the Computational Fluid Dynamics (CFD) simulation by Pallares *et al.*[24] over the same time span of 1.5 s. Solid and dashed lines for cases coded as B0 and B1, respectively, correspond to two separate simulations without and with considering buoyancy forces. In this last case the temperature difference between the exhaled flow ($T = 34$°C), and the ambient air ($T = 15$°C) is 19°C. The CFD simulations differed from the experiments both in the exhalation flow rate (max = 1.5 l/s) and also in the 3D model, in which the nasal cavity was not considered. Despite these differences, the CFD results are in good agreement with the experiments with absence of nasal flow. These results suggest a robust independence of the cloud trajectory on the exhalation flow rate and the relatively modest role of the buoyancy forces as defined in the CFD simulation.

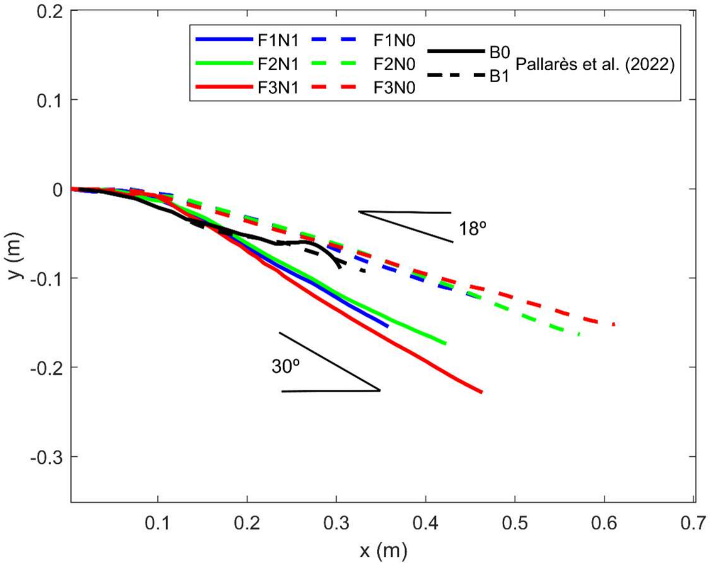

Figure 6. Ensemble-averaged trajectories of the centroid. The trajectories in black represent the centroid of the thermal fields with buoyancy (B1) and without buoyancy (B0) reported in Pallarès *et al.*[24].

Figure 7 (Multimedia available online) shows the effect of the nasal cavity on the particle cloud generated by a violent expiratory event under the same flow rate F3 during $t = 1.5$ s. As a reference, the coughs studied in Bourouiba *et al.*[10] using volunteers reached distances of about 0.7 m at $t = 0.34$ s, while in Tang *et al.*[3], the generated puff, also using volunteers, reached 0.6 m between $t = 0.5 - 2.5$ s. In the experiment shown in Figure 7, the distance is 0.7 m at $t = 0.67$ s. Additionally, Gupta *et al.*[6] characterized the angles, relative to the horizontal axis, of the particle cloud produced by of volunteer coughs. The measured upper and lower angles were $\theta_1 = 15 \pm 5°$ and $\theta_2 = 40 \pm 4°$, respectively. The angles extracted from Figure 7 in the case with closed nostrils are $\theta_1 = 10°$ and $\theta_2 = 30°$ aligning with the values observed in volunteer-based studies. Finally, to analyze the influence of the maximum flow rate and total duration of the expiratory event (shown in Table I) on the particle cloud, the rapid evolution toward the peak flow rate and subsequent sharp decrease directly affects the maximum distance reached by the particle cloud. In contrast, the total duration of the expiratory event dictates the total flow expelled but does not influence the shape or extent of the particle cloud`s trajectory.

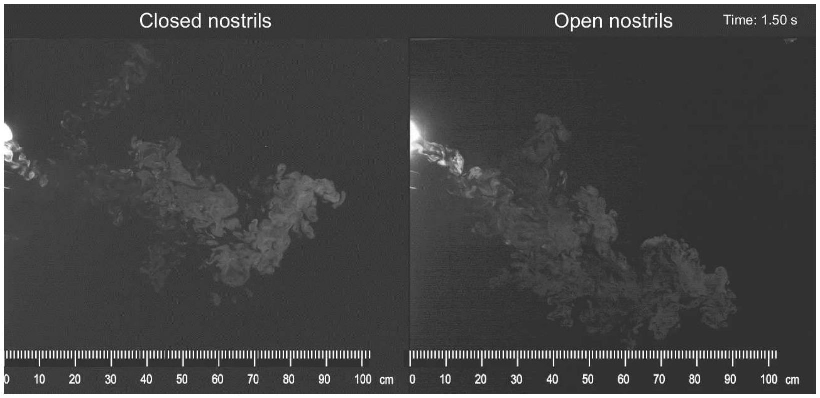

Figure 7. Videos Frames that show the effect of the nasal cavity on the particle cloud generated by a violent expiratory event under the same flow rate F3 at t = 1.5 s. The comparison between experiments for cases F3N0 (closed nostrils) and F3N1 (open nostrils) illustrates the significant influence of nasal flow on the particle cloud trajectory (Multimedia available online).

Figure 8 shows snapshots of 4 different realizations (in columns) containing images of the instantaneous particle clouds at $t = 0.5\ s$ for cases F1N0, F2N0 and F3N0 (in rows). Inspection of the images reveal a common and persistent flow feature in all cases in the form of a detached vortex ring traveling obliquely with respect to the main jet with an angle ranging between 30º and 80º with respect to the horizontal. To investigate the origin of this secondary flow we plotted in Figure 9 the time evolution of visualizations of the particle cloud for the cases F3N0 (a) and F3N1 (b). On the one hand, in panel a) initially the flow injection is essentially horizontal (see for example the visualization corresponding to $t = 0.02$ s and $t = 0.04$ s). As time increases, the flow is progressively oriented downwards by the effect of the bend generated by the larynx and the oral cavity as discussed in Pallares *et al.*[24]. This change in the flow direction, also shown in Figure 6 at $x \approx\ 0.1\ \mathrm{m}$, generates the detachment of a secondary vortex ring as illustrated by the snapshots shown in Figure 9 (a). On the other hand, the case F3N1 shown in panel b) do not develops a detachment of the vortex ring because of the nostril jets break this structure. Videos showing the temporal evolution during $t = 200\ \mathrm{ms}$ and detailed birth of the vortex ring in both cases (F3N0 and F3N1) are included in Figure 10 (Multimedia available online) respectively. Secondary flows originated by detached vortex ring have been reported in simulations of violent expiratory events[24,25] and in visualizations of turbulent puffs[26].

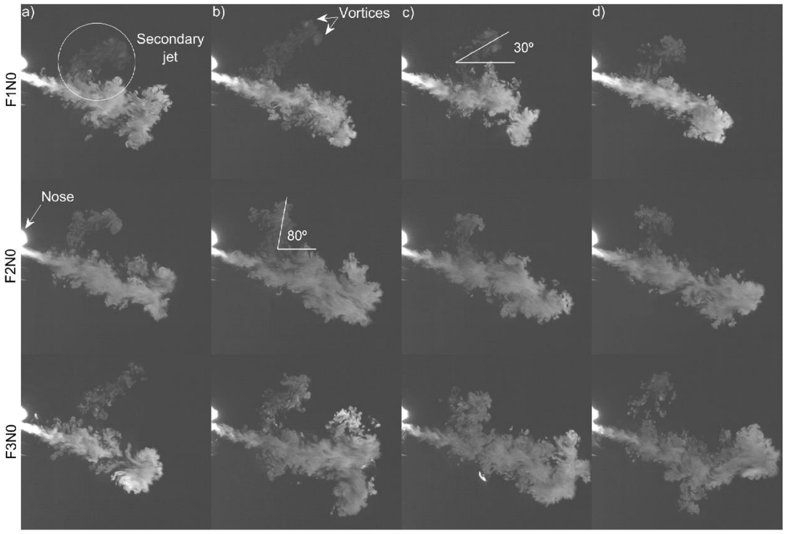

Figure 8. Snapshots at t = 0.5 s for 12 experiments showing the main jet and the vortex ring.

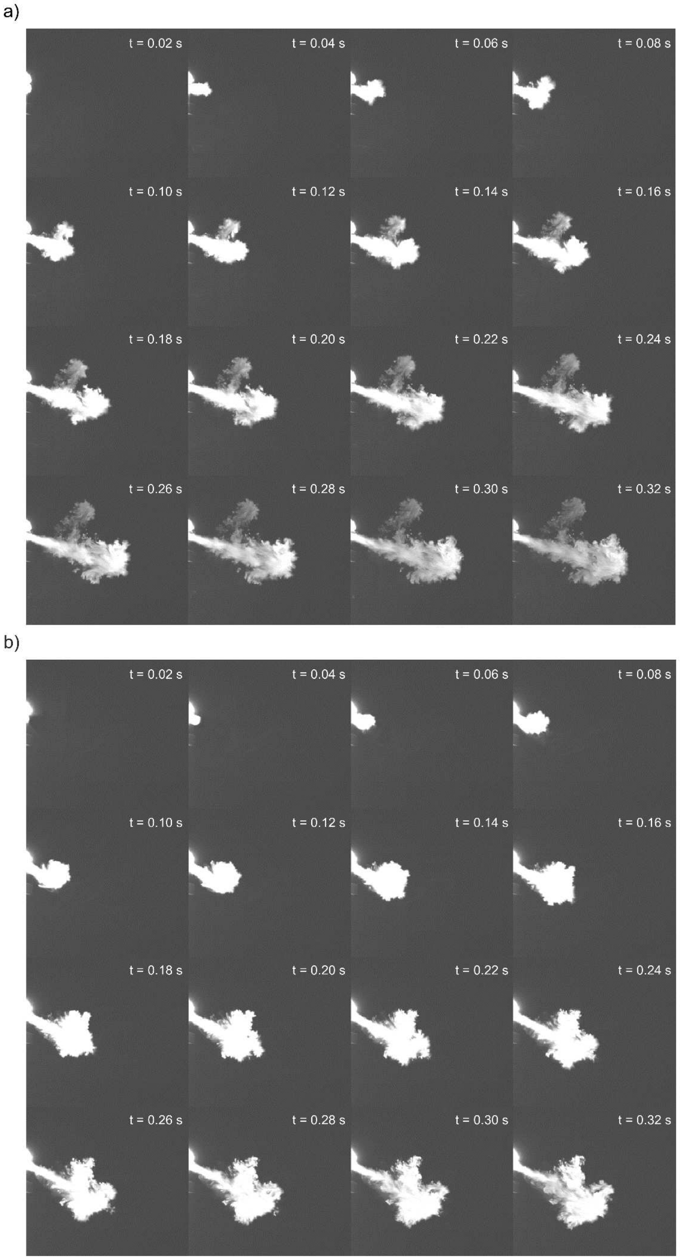

Figure 9. Birth and detailed evolution of the vortex ring in F3N0 (a) and F3N0 (b) at different time points.

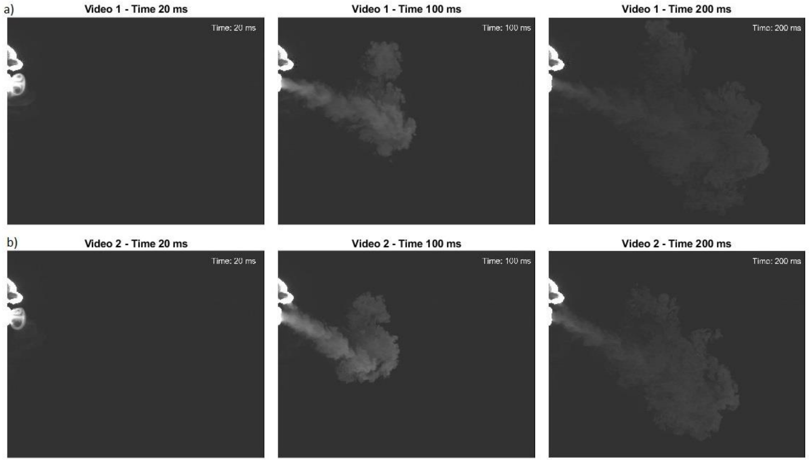

Figure 10. Videos frames of birth and detailed evolution of the vortex ring. (a) F3N0 case (Multimedia available online) and (b) F3N1 case (Multimedia available online) at three distinct time points: the initial time (20 ms) when the vortex ring forms, the middle time (100 ms), and the final time (200 ms).

3.2 Comparison with theoretical models

A model to predict the time evolution of the tip of a starting new jet derived by Abani and Reitz[27] was used to determine the range of the aerosol cloud generated in a violent expiratory event[21]. The model is based on the definition of the effective injection velocity to compute the time evolution of the position of the tip of the jet, given an entrainment coefficient K (see Appendix I for a detailed description of the theoretical model). As an example, Figure 11 shows the exit velocity at the mouth for cases F1N0 and F3N0 and the effective injection velocity used to compute the time evolution of the tip of the jet. It is evident that the effective injection velocity is slightly delayed with respect to the exit jet velocity with peak values damped by approximately 70%. Also, in comparison to the finite-time exit jet velocity, the effective injection velocity exhibits a monotonic decay well passed the end of the exit jet velocity.

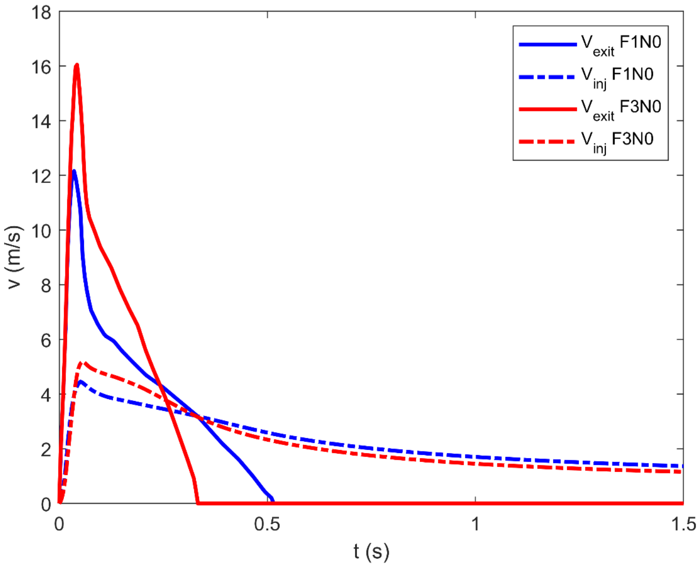

Figure 11. Time evolutions of the exit and injection velocities for cases F1N0 and F3N0.

Figure 12 shows an instantaneous binarized image of the particle cloud corresponding to the case F1N0 at $t = 0.75$ s. The position of the tip, x', is defined as the distance from the mouth to the jet front. We computed the time evolution of the entrainment coefficient K using Eq. 3, where $U_{inj,eff}(x',t)$ is the velocity of the tip and d_{eq} is the diameter equivalent (see Appendix I). The time evolutions of $\frac{dx'}{dt}$ and x' were determined by analyzing instantaneous binarized images as the one shown in Figure 12.

$$K = \frac{3U_{inj,eff}(x',t)d_{eq}}{\frac{dx'}{dt}x'} \tag{3}$$

PLEASE CITE THIS ARTICLE AS DOI: 10.1063/5.0241346

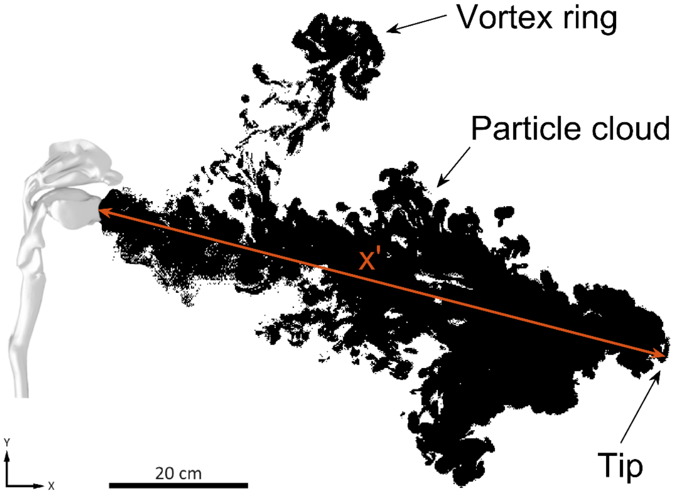

Figure 12. Particle cloud and vortex ring from a case with the nose closed F1N0 at t = 0.75 s.

As an example, Figure 13 shows the temporal evolution of the entrainment coefficient K obtained using Equation 3 for cases F1N1 (dashed blue line) and F3N1 (solid red line). These results show that K increases rapidly reaching its maximum value soon after the exhalation onset coinciding with the peak value of the exit velocity. For $t > 0.5$ s, K decreases back reaching a near constant value. Table III shows the averaged values of K at large times ($t > 0.5$) for the different cases considered. The values of the entrainment coefficient for each case are shown in Table III. Results suggest that the nasal flow increases the value of K while increasing the flow rate leads to decreasing entrainments. These results are in agreement with those reported by Ricout *et al.*[28] who found that K decreases as the injection Reynolds number is increased.

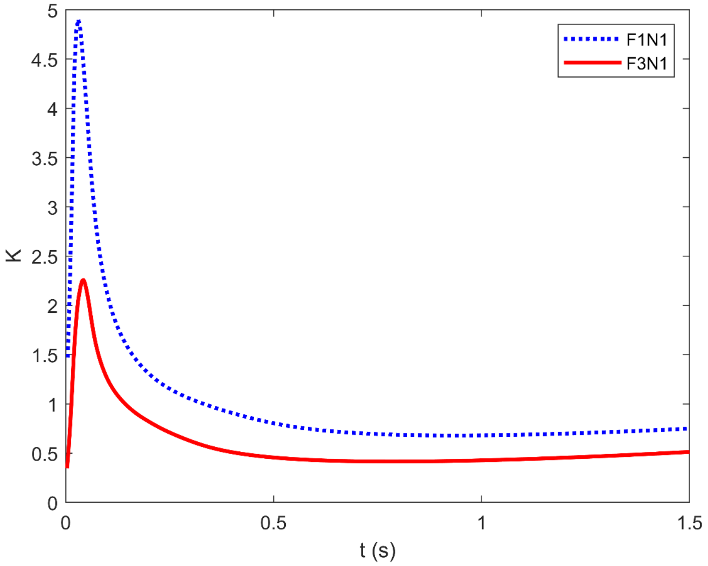

Figure 13. Computed time evolutions of the entrainment coefficients *K* for cases F1N1 and F3N1.

Figure 14 shows the temporal evolution of the experimental cloud tip, and the theoretical predictions obtained with the values of the entrainment coefficient in Table III. The agreement is good especially at large times, when time evolution of the entrainment coefficient reaches a plateau (see Fig. 13).

Code	α (°)	K
F1N0	18	0.60
F1N1	29	0.80
F2N0	18	0.45
F2N1	28	0.65
F3N0	16	0.37
F3N1	30	0.50

Table III. Time-averaged angle, with respect to the horizontal, of the centroid and entrainment coefficients for the different experimental conditions.

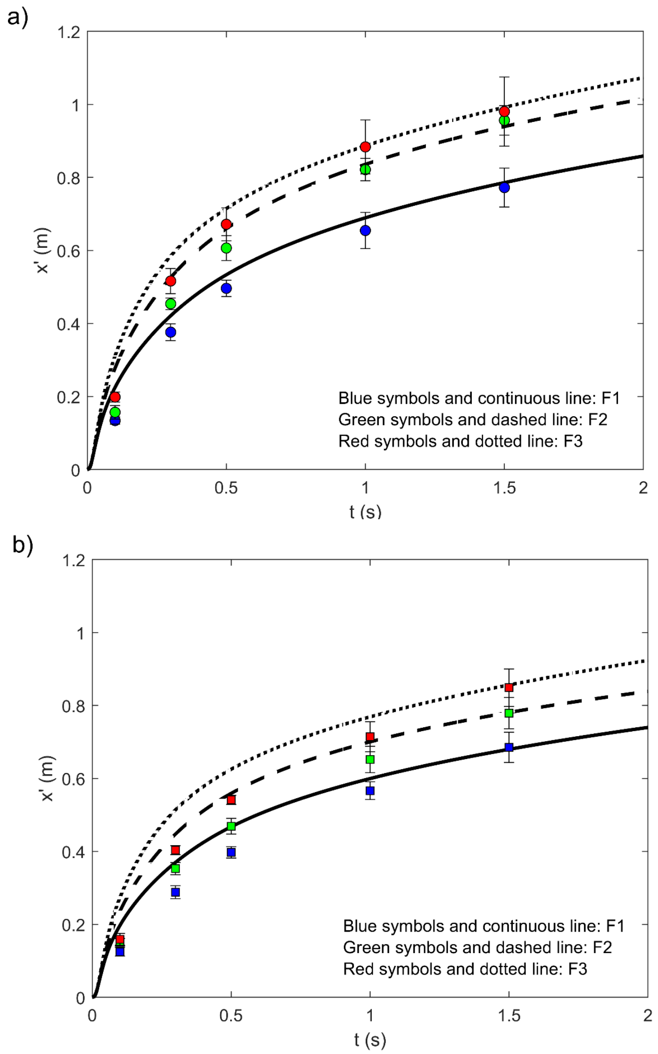

Figure 14. Time evolution of the range of the cloud along the direction of the centroid. Symbols correspond to the experiments and the lines to the theoretically predicted ranges. (a) Cases with the closed nostrils. (b) Cases with the open nostrils.

Using dimensional analysis, we plotted in Figure 15 the non-dimensional position of the tip of the jet as a function of the time scaled with the average flow exit velocity. Results indicate that all experimental measurement, comprising three flow rate values with and without nasal flow, collapse into a single curve. The best fit expression for this data, also shown in Figure 15 as a solid black line, is shown in the legend of the figure. This modified expression can be used to accurately predict the horizontal extent of a particle cloud generated by a violent respiratory event over the parameter space considered in this work regardless of the nasal flow effect.

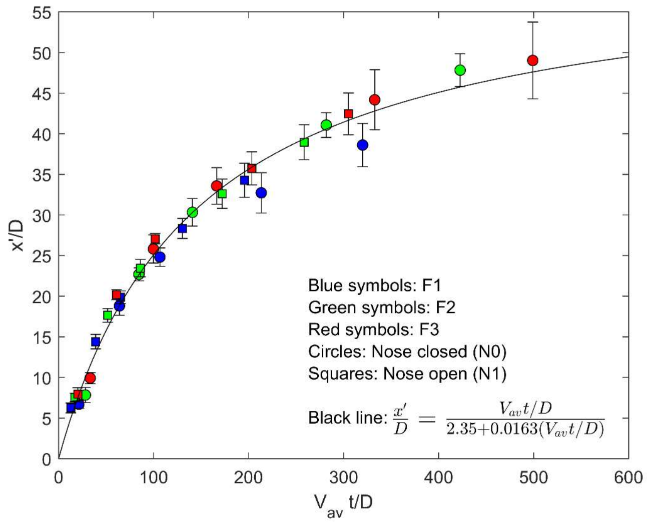

Figure 15. Non-dimensional time evolution of the range of the cloud along the direction of the centroid.

4.Conclusions

An experimental setup designed to reproduce an isothermal violent expiratory events using realistic upper respiratory tract has been designed and built to investigate the role of the exhalating flow rate and the existence of nasal flow on the resulting particle cloud trajectory and width. Specifically, we analyzed the dynamics of the aerosol cloud generated by three different flow rates over a duration of $t = 1.5\ s$, under both open and closed nostrils conditions. Results suggest that the nasal flow impacts the direction and the shape of the cloud significantly modifying the angle, with respect to the horizontal, of the trajectory of the cloud centroid. The trajectory of the centroid of the cloud has a downward angle of 18° with the closed nostrils and of 30° with the open nostrils. These values are essentially independent of the flow rate and the duration of the violent expiratory event. This highlights the critical role of the nasal cavity in shaping the dynamics of coughing and sneezing events. The peak velocity directly influences the distance travelled by the particle cloud, while the duration of the violent expiratory event does not affect either the distance or the shape of the particle cloud.

Flow visualizations revealed a vortex ring detaching upwards from the turbulent particle cloud in cases in which the nostrils were closed. This vortex ring structure was consistent across all flows, shedding approximately 10 cm from the mouth. The presence of the vortex ring is significant because it transports particles upwards, increasing the dispersion of potentially of pathogen-laden aerosols.

The theoretical model proposed by Pallares and Fabregat[21] with values of the entrainment coefficients measured in this study, accurately predicts the evolution of the tip of the particle cloud. The angles measured with respect to the horizontal axis in the experiments complement the direction of the particle cloud. Additionally, an expression derived from the experimental measurements of the tip of the particle cloud is provided to predict its evolution over time.

Real-world variables such as temperature and humidity have not been considered due to the limitations of our experimental setup. Although the temperature at the time studied does not have influence the evolution of the particle cloud, further studies at longer times are needed considering these variables.

By studying the behavior of the turbulent particle cloud, we gain valuable insights into the spread and infection mechanisms of respiratory diseases. These findings provide valuable insights into the influence of nasal airflow on aerosol dispersion. The downward deflection caused by nasal exhalation may reduce the horizontal spread but increases the vertical dispersion, suggesting that masks designed to block both nasal and oral pathways may significantly curb airborne transmission. This knowledge can inform the design of ventilation strategies in enclosed spaces such as restaurants, classrooms, hospitals, and transportation, among others. Optimizing ventilation systems based on particle cloud dynamics has the potential to significantly reduce the risk of airborne disease transmission.

Acknowledgments

This publication is part of the R&D&I projects PID2020-113303GB-C21 and PID2023-146648NB-C21, funded by MCIN/ AEI/10.13039/501100011033/ and "FEDER A way to do Europe", with the support of the Departament de Recerca i Universitats de la Generalitat de Catalunya, (ref. 2021SGR00732).

Author declarations

The authors have no conflicts to disclose.

Appendix I

In this Appendix we summarize the model proposed Abani and Reitz[27] to predict the time evolution of the axial position of the tip of a new jet. The equivalent diameter, d_{eq}, is defined as

$$d_{eq} = d_{noz}\sqrt{\frac{\rho_l}{\rho_g}} \tag{I1}$$

where $d_{noz} = 0.02\ m$ is the diameter of the nozzle where the flow is injected and ρ_l and ρ_g are the injected and surrounding fluid densities, respectively. In the isothermal case considered, $\rho_l = \rho_g$.

The velocity of the tip can be expressed as

$$\frac{dx'}{dt} = \frac{3U_{inj,eff}(x',t)d_{eq}}{Kx'} \tag{I2}$$

where x' is the position of the tip, $U_{inj,eff}(x',t)$ is the velocity of the jet tip, K is the entrainment coefficient. Ricout *et al.*[28] found that the values of K increase as the injection Reynolds number is reduced. Abani and Reitz[27] considered a constant value and assumed $K = 0.5$. On the other hand, Abraham[29] established typical values in the range $0.2 \leq K \leq 0.457$. Lastly, Pallares and Fabregat[21] fixed an entrainment coefficient $K = 0.24$ for the flow conditions corresponding to a mild cough. The integration of Equation I2 needs the definition of the initial position of the tip x'_0. According to Abani and Reitz[27] is defined as

$$x'_0 = \frac{3d_{eq}}{K} \tag{I3}$$

The time evolution of the effective injection velocity, $U_{inj,eff}(x',t)$, can be computed as,

$$U_{inj,eff}(x',t) = U_0 + \sum_{k=1}^{n} A(x',t-t_k)(\Delta U)_k \tag{I4}$$

$$A(x',t-t_k) = 1 - exp\left(-\frac{(t-t_k)}{\tau_{v,k}}\right) \tag{I5}$$

$$\tau_{v,k} = St\,\frac{x'}{U_k} \tag{I6}$$

where U_0 is the initial injection velocity, t is the current time, t_k is the previous time, $(\Delta U)_k = (U_k - U_{k-1})$ where U_k is the velocity injected at the nozzle, St is the Strouhal number. Abani and Reitz[27] considered a $St = 3$ because it was found to agree with results obtained from different injection profiles investigated in their study.

Appendix II

The parameters controlling the experimental setup are the set pressure in the pressurized tank and the angle of the ball valve. These variables influence the shape of the flow rate curve and the time duration, as shown in Figure 3 and summarized in Table I. To characterize the coughs and sneezes simulator, two pressures $P_1 = 200\ hPa$ and $P_2 = 250\ hPa$, and six angles of the ball valve, $\theta = \{42°, 45°, 48°, 50°, 53°, 58°\}$, were studied. These angles correspond to the degree of opening of the ball valve.

Figure II1 shows the evolution of peak flow rate (panel a) and total duration (panel b) as a function of the ball valve angle. It has been observed that the maximum flow rate decreases non-linearly as the angle of the ball valve increases (Figure II1 (a)). Conversely, the duration of the expiratory events follows a similar tends, showing a positive slope as illustrated in Figure II1 (b). These relationships correspond directly to the values plotted in Figure 3 and summarized in Table I.

The selection of the three flow rates were based on a combination of two variables: the set pressure in the pressurized tank, $P_1 = 200\ hPa$ and $P_2 = 250\ hPa$, and the ball valve angle, $\theta_1 = 45°$, $\theta_2 = 50°$, and $\theta_3 = 53°$. Flow rate F1 corresponds to $P_1\theta_3$, flow rate F2 to $P_2\theta_2$, and flow rate F3 to $P_2\theta_1$. For instance, flow rate F3 reached the maximum flow rate in the shortest time due to the combination of the higher pressure and the most open valve position.

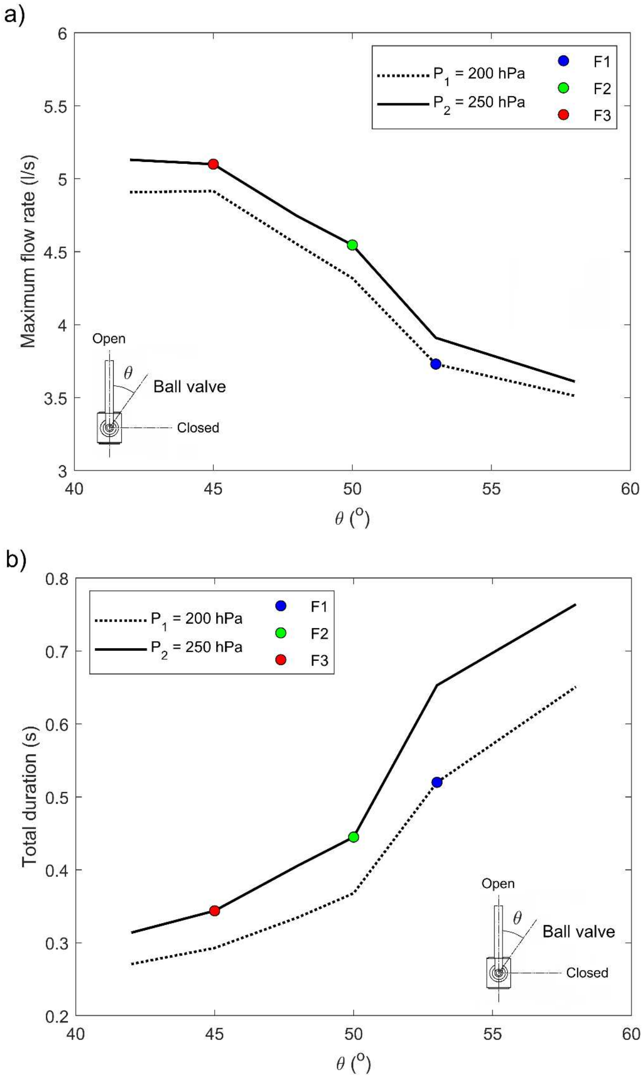

Figure II1. Relationship between the set pressure and ball valve angle. Panel (a) shows the evolution of the peak flow rate, while panel (b) illustrates the total duration of the expiratory event as a function of various ball valve angles.

References

1. Johns Hopkins Coronavirus Resource. Covid-19 map (2024). Available at: https://coronavirus.jhu.edu/map.html.

2. Tang, J. W. *et al.* Qualitative real-time schlieren and shadowgraph imaging of human exhaled airflows: An aid to aerosol infection control. *PLoS One* **6**, (2011).

3. Tang, J. W. *et al.* Airflow Dynamics of Human Jets: Sneezing and Breathing - Potential Sources of Infectious Aerosols. *PLoS One* **8**, (2013).

4. Arumuru, V., Pasa, J., Samantaray, S. S. & Varma, V. S. Breathing, virus transmission, and social distancing—An experimental visualization study. *AIP Advances* **11**, (2021).

5. Wang, C. C. *et al.* Airborne transmission of respiratory viruses. *Science* **373**, (2021).

6. Gupta, J. K., Lin, C. H. & Chen, Q. Flow dynamics and characterization of a cough. *Indoor Air* **19**, 517–525 (2009).

7. Bahl, P., de Silva, C. M., Chughtai, A. A., MacIntyre, C. R. & Doolan, C. An experimental framework to capture the flow dynamics of droplets expelled by a sneeze. *Experiments in Fluids* **61**, (2020).

8. Han, M. *et al.* Experimental measurements of airflow features and velocity distribution exhaled from sneeze and speech using particle image velocimetry. *Building and Environment* **205**, 108293 (2021).

9. Phuong, N. L. & Ito, K. Investigation of flow pattern in upper human airway including oral and nasal inhalation by PIV and CFD. *Building and Environment* **94**, 504–515 (2015).

10. Bourouiba, L., Dehandschoewercker, E. & Bush, J. W. M. Violent expiratory events: On coughing and sneezing. *Journal of Fluid Mechanics* **745**, 537–563 (2014).

11. Han, Z. Y., Weng, W. G. & Huang, Q. Y. Characterizations of particle size distribution of the droplets exhaled by sneeze. *Journal of The Royal Society Interface* **10**, (2013).

12. Chao, C. Y. H. *et al.* Characterization of expiration air jets and droplet size distributions immediately at the mouth opening. *Journal of Aerosol Science* **40**, 122–133 (2009).

13. Stiti, M., Castanet, G., Corber, A., Alden, M. & Berrocal, E. Transition from saliva droplets to solid aerosols in the context of COVID-19 spreading. *Environmental Research* **204**, (2022).

14. Lavrinenko, A., Fabregat, A., Gisbert, F. & Pallares, J. Direct numerical simulation of pathogen-laden aerosol dispersion in buoyancy-driven turbulent flow within

confined spaces. *International Communications in Heat and Mass Transfer* **152**, 107272 (2024).

15. Fabregat, A. *et al.* Direct numerical simulation of turbulent dispersion of evaporative aerosol clouds produced by an intense expiratory event. *Physics of Fluids* **33**, (2021).

16. Fontes, D., Reyes, J., Ahmed, K. & Kinzel, M. A study of fluid dynamics and human physiology factors driving droplet dispersion from a human sneeze. *Physics of Fluids* **32**, (2020).

17. Zhao, K., Blacker, K., Luo, Y., Bryant, B. & Jiang, J. Perceiving nasal patency through mucosal cooling rather than air temperature or nasal resistance. *PLoS One* **6**, e24618 (2011).

18. Shim, G., Narayanan, S. R. & Yang, S. Numerical simulation of virus-laden aerosol transmission in real human respiratory airways. *Physics of Fluids* **35**, (2023).

19. Shang, Y. & Inthavong, K. Numerical assessment of ambient inhaled micron particle deposition in a human nasal cavity. *Experimental and Computational Multiphase Flow* **1**, 109–115 (2019).

20. Islam, M. S. *et al.* How SARS-CoV-2 Omicron droplets transport and deposit in realistic extrathoracic airways. *Physics of Fluids* **34**, (2022).

21. Pallares, J. & Fabregat, A. A model to predict the short-term turbulent indoor dispersion of small droplets and droplet nuclei released from coughs and sneezes. *Indoor and Built Environment* **31**, 1393–1404 (2022).

22. ERCOFTAC. Description AC7-01. (2024). Available at: https://www.kbwiki.ercoftac.org/w/index.php?title=Description_AC7-01.

23. Brüning, J. *et al.* Characterization of the Airflow within an Average Geometry of the Healthy Human Nasal Cavity. *Scientific Reports* **10**, (2020).

24. Pallares, J., Fabregat, A. & Cito, S. Effects of upper respiratory tract anatomy and head movement on the buoyant flow and particle dispersion generated in a violent expiratory event. *Journal of Aerosol Science* **166**, 106052 (2022).

25. Trivedi, S. *et al.* Estimates of the stochasticity of droplet dispersion by a cough. *Physics of Fluids* **33**, (2021).

26. Scorer R S. *Dynamics of Meteorology and Climate*. (1997).

27. Abani, N. & Reitz, R. D. Unsteady turbulent round jets and vortex motion. *Physics of Fluids* **19**, (2007).

28. Ricout, F. P. & Spalding, D. B. Measurements of Entrainment by Axisymmetrical Turbulent Jets. *Journal of Fluid Mechanics* **11**, 21-32 (1961).

29. Abraham, J. Entrapment characteristics of transient gas jets. *Numerical Heat Transfer, Part A: Applications* **30**, 347–364 (1996).